

Reflectance and Texture of Real-World Surfaces

KRISTIN J. DANA

Columbia University

BRAM VAN GINNEKEN

Utrecht University

SHREE K. NAYAR

Columbia University

JAN J. KOENDERINK

Utrecht University

In this work, we investigate the visual appearance of real-world surfaces and the dependence of appearance on the geometry of imaging conditions. We discuss a new texture representation called the BTF (bidirectional texture function) which captures the variation in texture with illumination and viewing direction. We present a BTF database with image textures from over 60 different samples, each observed with over 200 different combinations of viewing and illumination directions. We describe the methods involved in collecting the database as well as the importance and uniqueness of this database for computer graphics. A related quantity to the BTF is the familiar BRDF (bidirectional reflectance distribution function). The measurement methods involved in the BTF database are conducive to a simultaneous measurement of the BRDF. Accordingly, we also present a BRDF database with reflectance measurements for over 60 different samples, each observed with over 200 different combinations of viewing and illumination directions. Both of these unique databases are publicly available and have important implications for computer graphics.

Categories and Subject Descriptors: I.2.10 [**Artificial Intelligence**]: Vision and Scene Understanding—intensity, color, *photometry*, and *thresholding*; *texture*; I.3.5 [**Computer Graphics**]: Computational Geometry and Object Modeling—*physically based modeling*; I.4.1 [**Image Processing and Computer Vision**]: Digitization and Image Capture—*imaging geometry*; *radiometry*, *reflectance*; I.4.7 [**Image Processing and Computer Vision**]: Feature Measurement—*texture*; I.4.8 [**Image Processing and Computer Vision**]: Scene Analysis—*photometry*

General Terms: Experimentation, Measurement

The research is sponsored in part by the National Science Foundation, DARPA/ONR under the MURI Grant No. N00014-95-1-0601 and by REALISE of the European Commission.

Authors' addresses: K. J. Dana, S. K. Nayar, Department of Computer Science, Columbia University, New York, NY 10027; email: <{dananayar}@cs.columbia.edu>; B. van Ginneken, Image Sciences Institute, University Hospital Utrecht, 3584 CX Utrecht, The Netherlands; email: <bram@isi.uu.nl>; J. J. Koenderink, Department of Physics, Utrecht University, 3508 TA Utrecht, The Netherlands; email: <koenderink@phys.uu.nl>.

Permission to make digital/hard copy of part or all of this work for personal or classroom use is granted without fee provided that the copies are not made or distributed for profit or commercial advantage, the copyright notice, the title of the publication, and its date appear, and notice is given that copying is by permission of the ACM, Inc. To copy otherwise, to republish, to post on servers, or to redistribute to lists, requires prior specific permission and/or a fee.

© 1999 ACM 0730-0301/99/0100–0001 \$5.00

Additional Key Words and Phrases: Bidirectional reflectance distribution function, bidirectional texture function, “3D texture”

1. INTRODUCTION

Characterizing the appearance of real-world textured surfaces is a fundamental problem in computer vision and computer graphics. Appearance depends on view, illumination, and the scale at which the texture is observed. At coarse scale, where local surface variations are subpixel and local intensity is uniform, appearance is characterized by the BRDF (bidirectional reflectance distribution function). At fine scale, where the surface variations give rise to local intensity variations, appearance can be characterized by the BTF (bidirectional texture function). As a direct analogy to the BRDF, we have introduced the term BTF to describe the appearance of texture as a function of illumination and viewing direction. Specifically, the BTF is a texture image parameterized by the illumination and viewing angles. This taxonomy is illustrated in Figure 1.

Studying the dependence of texture on viewing and illumination directions is fairly new in texture research and so there is only a limited amount of related work. For example, Koenderink and van Doorn [1996] discuss the issues involved in texture due to surface geometry, Stavridi et al. [1997] measure the variation of brick texture with imaging conditions,Debevec et al. [1996] incorporate a type of view-dependent texture for rendering architecture and Leung and Malik [1997] consider perpendicular texture comprised of elements normal to the surface. Our work in addressing the problem has resulted in two publicly available databases: a BTF measurement database with texture images from over 60 different samples, each observed with over 200 combinations of viewing and illumination directions and a BRDF measurement database with reflectance measurements from the same 60 samples. Each of these databases is made publicly available at www.cs.columbia.edu/CAVE/curet. In this article, we provide a detailed description of the database contents and measurement procedure. The database has generated substantial interest since it first became available [Dana et al. 1996]. This interest is evident in the numerous works using the database: BRDF model-fitting in Dana et al. [1996, 1997] and Koenderink et al. [1998], histogram simulations in Ginneken et al. [1997], a histogram model and histogram model-fitting in Dana and Nayar [1998], and SVD (singular value decomposition) analysis in Suen and Healey [1998].

The BTF database, comprised of over 14,000 images, can be used for development of 3-D texture algorithms. In computer graphics, traditional methods of 2-D texture synthesis and texture-mapping make no provision for the change in texture appearance with viewing and illumination directions. For example, in 2-D texture-mapping when a single digital image of a rough surface is mapped onto a 3-D object, the appearance of roughness is usually lost or distorted. Bump-mapping [Blinn 1977, 1978; Becker and

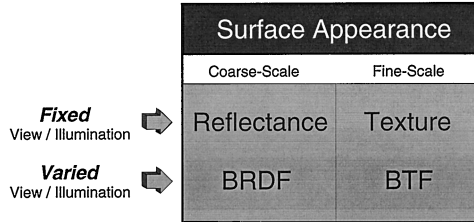


Fig. 1. Taxonomy of surface appearance. When viewing and illumination directions are fixed, surface appearance can be described by either reflectance (at coarse-scale observation) or texture (at fine-scale observation). When viewing and illumination directions vary, the equivalent descriptions are the BRDF and the BTF. Analogous to the BRDF, BTF is a function of four independent angles (two each for viewing and illumination directions).

Max 1993] preserves some of the appearance of roughness, but knowledge of the surface shape is required and shadows cast from the local surface relief are not rendered. Many of the problems associated with traditional texture-mapping and bump-mapping techniques are described in Konderink and van Doorn [1996]. If the exact geometry of the surface is known, ray tracing can be used but at a high computational cost. Another method of rendering surface texture is solid texturing,¹ which combines a volumetric texture synthesis with volume rendering techniques. This method is computationally intensive and is applicable for a limited variety of textures. With the availability of the BTF database, the potential exists for 3-D texturing algorithms using images, without the need for a volumetric texture model or surface synthesis procedure.

In computer vision, current texture algorithms such as shape-from-texture, texture segmentation, and texture recognition are appropriate for textures that arise from albedo or color variations on smooth surfaces.² In contrast, the texture due to surface roughness has complex dependencies on viewing and illumination directions. These dependencies cannot be studied using existing texture databases that include few images or a single image of each sample (for instance, the widely used Brodatz database). Our texture database covers a diverse collection of rough surfaces and captures the variation of image texture with changing illumination and viewing directions. This BTF database is a first step towards extending current texture analysis algorithms to include texture from nonsmooth real-world surfaces.

Although the BTF is a new framework for the study of texture, the BRDF has been around for decades. The BRDF was first defined in 1970 by Nicodemus [1970] and Nicodemus et al. [1977] as the scattered surface radiance (in units of watts per unit area per unit solid angle) divided by the incident surface irradiance (in units of watts per unit area). Interest in measuring the BRDF spans many fields including optical engineering, remote-sensing, computer vision, and computer graphics. In optical engi-

¹Please see Peachey [1985], Perlin [1989, 1985], Lewis [1989], and Sakas and Kernke [1994].

²Please see Chatterjee [1993], Kashyap [1984], Krumm and Shafer [1995], Patel and Cohen [1992], Super and Bovik [1995], Wang and Healey [1996], and Xie and Brady [1996].

neering, the BRDF of components is a critical design issue. Optical scatter is considered a source of noise that limits system resolution and throughput [Stover 1989]. In the development of space optics, scatter from contaminants (such as rocket exhaust) is a key issue in system development [Stover 1989; Herren 1989; Howard et al. 1989]. In other fields, the BRDF is needed not to measure contamination of simple optical surfaces, but rather to understand the inherently complex optical behavior of natural surfaces. In remote-sensing, the BRDF of terrestrial surfaces such as soil, vegetation, snow, and ice is a popular research topic.³ Here, there is a need to distinguish changes in imaging parameters from changes due to target variations (different soil type, change in vegetation, change in soil moisture, etc.). In computer vision, the reflectance from a surface can be used to determine 3-D shape such as in shape-from-shading [Horn and Brooks 1989] or photometric stereo [Woodham 1980]. In order for such algorithms to function properly, the BRDF must be well modeled which can be verified via measurement. In computer graphics, the BRDF has a clear application in the rendering of realistic surfaces.

Although BRDF models have been widely discussed and used in computer vision and computer graphics,⁴ the BRDFs of a large and diverse collection of real-world surfaces have never before been available. Our measurements comprise a comprehensive BTF/BRDF database (the first of its kind) that is now publicly available. Our measurement procedure does not employ a gonioreflectometer or the hemispherical mirror arrangement described in Ward [1992]. Instead, a robotic manipulator and CCD camera are employed to allow simultaneous measurement of the BTF and the BRDF of large samples (about 10×10 cm). Exactly how well the BRDFs of real-world surfaces fit existing models has remained unknown as each model is typically verified using a small number (two to six) of surfaces. Our large database allows researchers to evaluate the performance of existing and future BRDF models and representations.

2. MEASUREMENT METHODS

2.1 Measurement Device

Our measurement equipment depicted in Figure 2 is comprised of a robot,⁵ lamp,⁶ personal computer,⁷ photometer,⁸ and video camera.⁹ Measuring the

³Please see Sandmeier et al. [1995], Nolin et al. [1994], Li et al. [1994], and Schluessel et al. [1994].

⁴Please see Westin et al. [1992], Torrance and Sparrow [1967], Poulin and Fournier [1990], Ward [1992], Nayar et al. [1991], Tagare and DeFigueiredo [1993], Wolff [1994], Koenderink et al. [1996, 1998], Oren and Nayar [1995], and van Ginneken et al. [1998].

⁵SCORBOT-ER V by ESHED Robotec (Tel Aviv, Israel).

⁶Halogen bulb with a Fresnel lens.

⁷IBM compatible PC running Windows 3.1 with "Videomaker" frame grabber by VITEC Multimedia.

⁸SpectraScan PR-704 by PhotoResearch (Chatsworth, CA).

⁹Sony DXC-930 3-CCD color video camera.

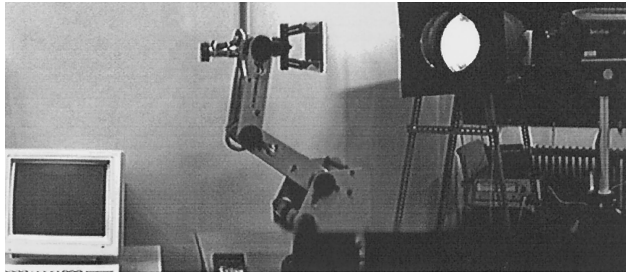


Fig. 2. Measurement setup. The equipment consists of a personal computer with a 24-bit RGB frame grabber, a robot arm to orient the texture samples, a halogen bulb with a Fresnel lens which produces a parallel beam, a photometer, and a 3-CCD color video camera (not shown).

BRDF requires radiance measurements for a range of viewing/illumination directions. For each sample and each combination of illumination and viewing directions, an image from the video camera is captured by the frame grabber. These images have 640×480 pixels with 24 bits per pixel (8 bits per RGB channel). The pixel values are converted to radiance values using a calibration scheme described in Section 2.3. The calibrated images serve as the BTF measurements and these images are averaged over the sample area to obtain the BRDF measurements, as illustrated in Figure 3.

The need to vary the viewing and light source directions over the entire hemisphere of possible directions presents a practical obstacle in the measurements. This difficulty is reduced considerably by orienting the sample to generate the varied conditions. As illustrated in Figure 4, the light source remains fixed throughout the measurements. The light rays incident on the sample are approximately parallel and uniformly illuminate the sample. The camera is mounted on a tripod and its optical axis is parallel to the floor of the lab. During measurements for a given sample, the camera is moved to seven different locations, each separated by 22.5 degrees in the ground plane at a distance of 200cm from the sample. For each camera position, the sample is oriented so that its normal is directed toward the vertices of the facets that tessellate the fixed quarter-sphere illustrated in Figure 4.¹⁰ With this arrangement, a considerable number of measurements are made in the plane of incidence (i.e., illumination direction, viewing direction, and sample normal lie in the same plane). Also, for each camera position, a specular point is included where the sample normal bisects the angle between the viewing and illumination directions. Sample orientations with corresponding viewing angles or illumination angles greater than 85 degrees are excluded from the measurements to avoid self-occlusion and self-shadowing. This exclusion results in the collection of 205 images for each sample with 55 images taken at camera position 1, 48

¹⁰The vertices of the quarter sphere shown in Figure 4(a) were obtained by starting with the two triangles formed by the coordinates $(1,0,0)$, $(0,0,1)$, $(0,-1,0)$, and $(0,1,0)$ and then barycentrically subdividing.

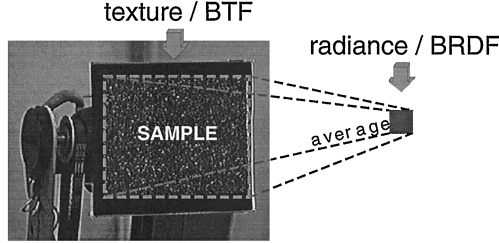


Fig. 3. Sample (roofing shingle) mounted on a robot. The average intensity over the sample is the radiance or BRDF measurement and the image of the sample is the texture or BTF measurement for a particular viewing and light source direction.

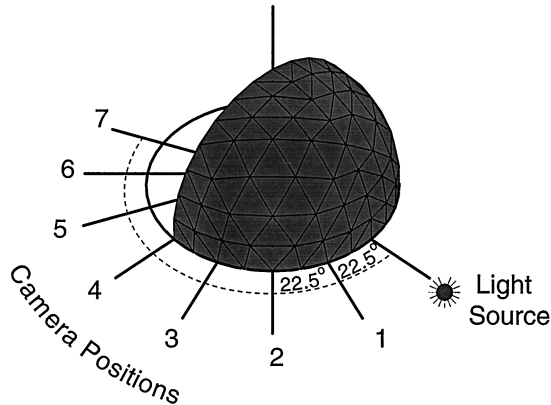


Fig. 4. The vertices on the hemisphere correspond to the directions to which the robot orients the sample's surface normal. The illumination direction remains fixed and the camera is positioned in seven different locations in a plane. These seven locations correspond to angular deviations of 22.5° , 45° , 67.5° , 90° , 112.5° , 135° , 157.5° from the light source direction. For each camera position, images of the sample are acquired at the subset of sample orientations that are visible and illuminated. The total number of images acquired per sample is 205.

images at position 2, 39 images at position 3, 28 images at position 4, 19 images at position 5, 12 images at position 6, and 4 images at position 7. A complete table of sample orientations is given in the online database.

Figure 5 shows an alternative representation of the 205 measurements for each sample. Here, the illumination directions are shown in the sample coordinate frame $\mathbf{x}_s\text{-}\mathbf{y}_s\text{-}\mathbf{z}_s$. Notice that the illumination directions are evenly distributed over the quarter-sphere so the set of all possible illumination directions is well represented by the subset used in the measurements. To determine which viewing directions are paired with each of these illumination directions, consider that each distinct illumination direction corresponds to a distinct sample orientation. Consequently, there are a maximum of seven viewing directions for each illumination direction, corresponding to the seven camera positions. There can be less than seven viewing directions for a given illumination direction because a particular combination of sample orientation and camera position is excluded if the corresponding viewing direction is greater than 85 degrees from the sample

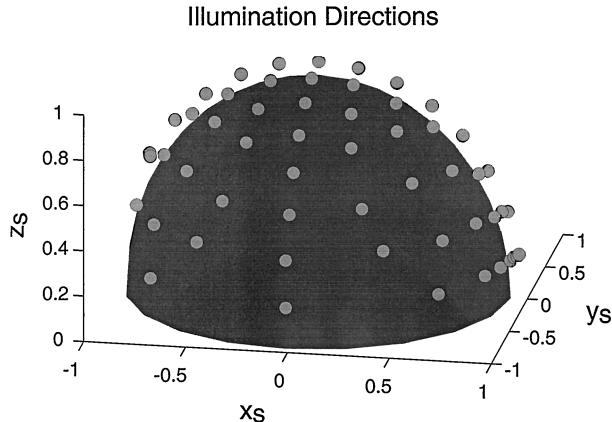


Fig. 5. An alternative interpretation of the measurements described in Figure 4. Illumination directions are shown in the sample coordinate frame. The sample lies in the \mathbf{x}_s - \mathbf{y}_s plane and its global normal points in the direction of \mathbf{z}_s . Each circular marker represents a distinct illumination direction. For each of these illumination directions, the sample is imaged from seven viewing directions, corresponding to the seven camera positions shown in Figure 4.

normal. Figure 6 shows examples of illumination directions with their associated viewing directions.

For anisotropic textures, the 205 measurements are repeated after rotating the sample about \mathbf{z}_s by either 90 degrees or 45 degrees depending on the structure of the anisotropy. For example, the linen sample was rotated by 45 degrees because its horizontal and vertical threadings form a gridlike structure that does not change when rotated by 90 degrees. On the other hand, the sample of corduroy was rotated by 90 degrees to obtain the maximum difference in surface structure. The anisotropic textures were Sample 38 (ribbed paper), Sample 40 (straw), Sample 42 (corduroy), Sample 44 (linen), Sample 46 (cotton), Sample 51 (corn husk), Sample 54 (wood_a), Sample 56 (wood_b), and Sample 58 (tree bark).

2.2 Samples for Measurements

The collection of real-world surfaces used in the measurements is illustrated in Figure 7. Samples of these surfaces were mounted on $10 \times 12\text{cm}$ bases that were constructed to fit onto the robot gripper. Each sample, though globally planar, exhibits considerable depth variation or macroscopic surface roughness. The samples were chosen to span a wide range of geometric and photometric properties. The categories include specular surfaces (aluminum foil, artificial grass), diffuse surfaces (plaster, concrete), isotropic surfaces (cork, leather, styrofoam), anisotropic surfaces (straw, corduroy, corn husk), surfaces with large height variations (crumpled paper, terry cloth, pebbles), surfaces with small height variations (sandpaper, quarry tile, brick), pastel surfaces (paper, cotton), colored surfaces (velvet, rug), natural surfaces (moss, lettuce, fur) and manmade surfaces (sponge, terry cloth, velvet).

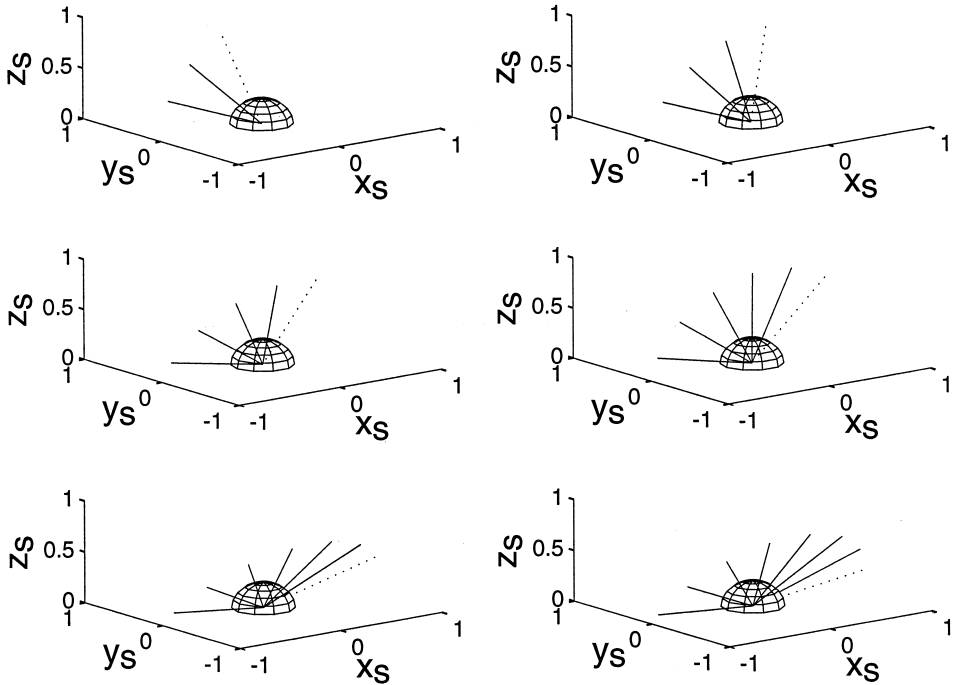


Fig. 6. Viewing directions in the sample coordinate frame. For each illumination direction shown in Figure 5, there are at most seven associated viewing directions corresponding to the seven camera positions. Each panel shows an example of an illumination direction (dotted line) and the associated viewing directions (solid lines). The viewing directions lie in a plane that changes with illumination direction. Since the sample is not visible for every camera position, the number of associated viewing conditions also varies with illumination direction. The plots show examples of illumination directions with two to seven associated viewing directions.

2.3 Radiometric Calibration

Radiometric calibration is performed to interpret pixel values as radiance. This calibration is done by measuring radiance from the samples and from a Kodak standard card¹¹ (illustrated in Figure 8) using a photometer.¹² We refer to the radiance measurements and pixel values from the Kodak standard card as the *standard calibration data*. The radiance measurements and pixel values from the sample are termed *sample calibration data*.

2.3.1 Standard Calibration Data. To obtain the standard calibration data, the standard card shown in Figure 8 is placed in the robotic sample holder. The card has 20 gray strips with 0.1 density increments and relative density values from a nominal “white” of approximately 0.05 (90% reflectance) to 1.95 (1% reflectance). In addition, the card has 12 colored-strips with two shades of blue, cyan, green, yellow, red, and magenta. The

¹¹Kodak Color Separation Guide and Gray Scale, Kodak Publication No. Q-13.

¹²SpectraScan PR-704 by Photoresearch (Chatsworth, CA).



Fig. 7. The collection of 61 real-world surfaces used in the measurements. The name and number of each sample is indicated above its image. The samples were chosen to span a wide range of geometric and photometric properties. Different samples of the same type of surfaces are denoted by letters, for example, Brick_a and Brick_b. Samples 29, 30, 31, and 32 are close-up views of samples 2, 11, 12, and 14, respectively.

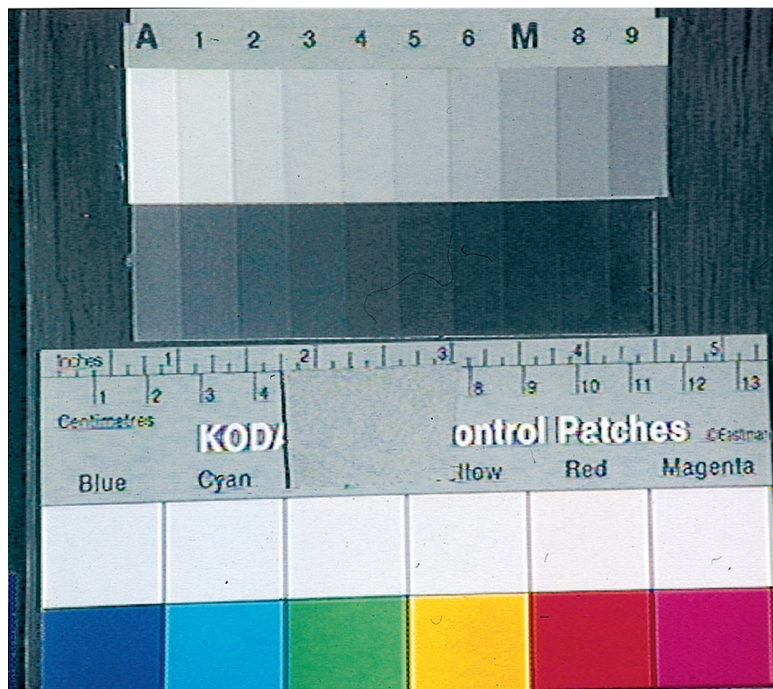


Fig. 8. Kodak standard card with 20 strips of gray and 12 color strips.

sample holder is oriented so that the card is frontal to the lamp. The photometer is placed in camera position 1, 22.5° from the lamp as illustrated in Figure 4. The photometer has a circular region of interest (0.8cm in diameter) marked in its viewfinder to identify the position on the card from which the radiance is measured. To obtain the standard calibration data, the photometer is oriented so that its region of interest is positioned within each strip on the standard card. The photometer records 200 radiance values, corresponding to the radiance in watts/(steridian – meter²) for each 2nm interval between the wavelengths 380nm and 780nm. The recording of radiance values from the standard card does not have to be done for every day of the measurement procedure. In theory, the radiance need only be measured once for each lamp used in the experiment. However, to keep track of the slowly decreasing intensity of a particular lamp over the course of the experiment, the recordings were made more than once for each lamp. See Appendix A for a discussion.

To relate radiance to pixel values, an image of the standard card must be obtained as well. Since the camera settings can vary for each sample, an image of the standard card is obtained for every sample measured. After the lens aperture and camera settings are adjusted for each sample, the image of the standard card is recorded. The pixels in each strip (isolated by manual segmentation) are averaged. Since there are 32 strips on the card (20 gray and 12 color), the standard calibration data are 32 radiance values with corresponding pixel values.

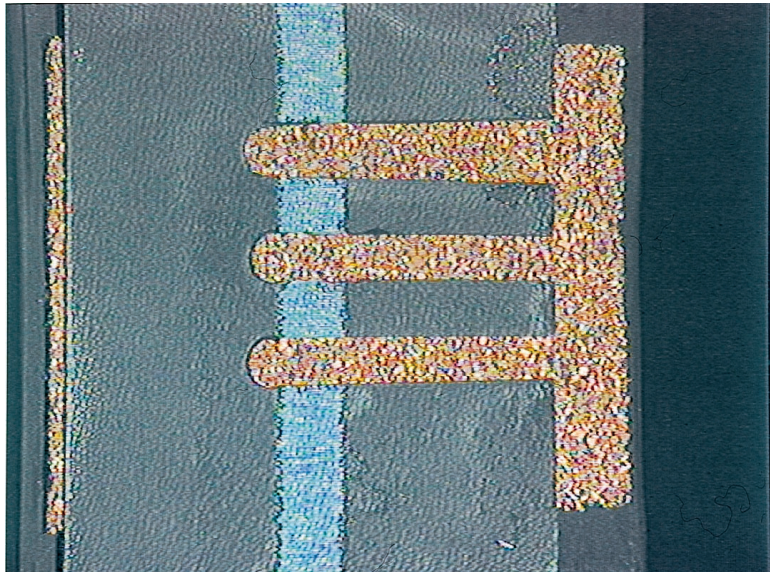


Fig. 9. Fiducial marker attached to sample. This metallic grid with painted stripe is used as a fiducial marker to specify a spatial region for measuring radiance with the photometer and recording pixel values with the video camera. These radiance and pixel measurements are used in radiometric calibration.

2.3.2 Sample Calibration Data. Sample calibration data (i.e., radiance and pixel values taken from the sample) are useful because calibration is likely to be wavelength dependent. That is, the relationship between radiance and pixel values is likely to depend on the wavelength of interest. Since the wavelength of interest is determined by the color of the sample, it makes sense to calibrate using reflectance values from the sample. Standard calibration data are used in conjunction with sample calibration data because the standard calibration data often cover the range of the operating curve better than the sample calibration data especially in the case of dark samples.

To determine the relationship between radiance and pixel values an operating curve is needed, where the radiance and pixel values are recorded over a range of reflected intensity. For the standard calibration data, this range of measurements was obtained via the varying reflectance values of the gray reference strips. For the sample data we varied the angle between the light source and the sample normal (keeping the sample normal in the plane of incidence) to obtain a range of bright and dark intensity values.

When recording the sample calibration data, a fiducial marker is necessary to localize the region where pixel values and photometer readings are obtained. We use a metal grid that fits over the sample as the fiducial marker, as illustrated in Figure 9. The circular photometer region (0.8cm diameter) is positioned so that its center diameter aligns with the right edge of the grid line. For eight sample orientations, three radiance and

pixel values are obtained corresponding to the three slit openings of the grid. The eight sample orientations correspond to the light source direction and the directions of camera positions 1 through 7. These orientations were chosen so that bright and dark points would be included in the sample calibration data.

We use two methods for radiometric calibration. In both methods the relationship between radiance and associated pixel value is approximated as linear. The first method, termed *gray calibration*, relates the average of the red, green, and blue pixels to the total radiance recorded by the photometer (i.e., radiance from the wavelength range 380nm to 780nm). Letting r denote the total radiance and p denote the average pixel value, the parameters estimated are a and b where

$$r = a * p + b. \quad (1)$$

The gray calibration results are illustrated in Figure 19 of Appendix C.

The second method, termed *color calibration*, estimates the camera sensitivity curves for the red, green, and blue CCD of the video camera. The average radiance for the red, green, and blue spectral regions is obtained by integrating the estimated sensitivity curves multiplied by the radiance per wavelength (as measured by the photometer). The relationship between the RGB pixels and the corresponding RGB radiance is assumed linear. The sensitivity function is assumed to be a unit area Gaussian function. For each sample, the mean and variance of this Gaussian function is estimated along with the linear radiometric calibration curves through nonlinear estimation. The resulting mean and variances over all samples are averaged to obtain the final estimates of the sensitivity curves. These estimated sensitivity curves, depicted in Figure 10, were used to obtain the final estimate for the linear relationships between the RGB pixel values and RGB radiance for each sample. Let r_r , r_g , and r_b denote the red, green, and blue radiance, respectively, and let p_r , p_g , and p_b denote the red, green, and blue pixel values, respectively. Then the color calibration method estimates a_r , b_r , a_g , b_g , a_b , and b_b , where

$$r_r = a_r * p_r + b_r, \quad (2)$$

$$r_g = a_g * p_g + b_g, \quad (3)$$

$$r_b = a_b * p_b + b_b. \quad (4)$$

The color calibration results are illustrated in Figure 20 of Appendix C.

In both the gray and color calibration methods the data are not always weighted equally. Sample calibration data are weighted more than the standard calibration except when the sample calibration data suffer from underflow or overflow. Data with significant pixel underflow (pixel values near zero) or overflow (pixel values near 255) are not used.

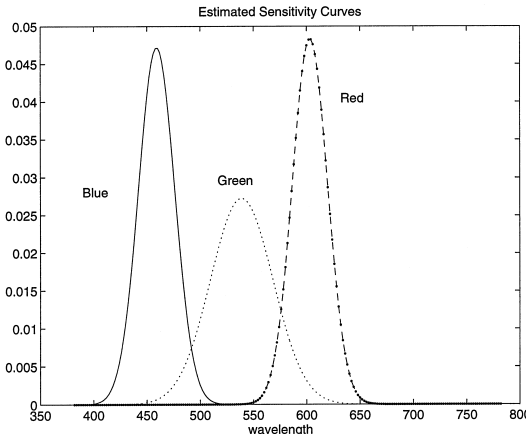


Fig. 10. The estimated sensitivity curve for the 3-CCD color video camera. The mean and standard deviation for the red sensitivity curve were 604nm and 16.6nm, respectively. The mean and standard deviation for the green sensitivity curve were 538nm and 29.2nm, respectively. The mean and standard deviation for the red sensitivity curve were 460nm and 17nm, respectively. Note that each estimated sensitivity curve is normalized to have unit area.

2.4 Measurement Procedure

The general steps of the measurement procedure have been discussed in previous sections. The purpose of this section is to clarify the procedure by listing the steps in chronological order as follows.

Adjust camera aperture. Place camera in Position 1 and place current sample in sample holder on robotic manipulator. Orient sample so that it appears very bright (for most samples this will occur either in a position frontal to the lamp or a specular position) and adjust the aperture to minimize pixel overflow. Orient the sample so that it appears quite dark (e.g., at an orientation far from the light source direction) and adjust the aperture to reduce pixel underflow. This process is repeated until a reasonable aperture size for the current sample is obtained. Pixel overflow and underflow are rarely eliminated completely and contribute to the sources of error as discussed in Appendix B.

Record a reference image of gray card. The sample is replaced with a Kodak 18% gray card¹³ cut to sample size (10 × 12cm). An image of this card is recorded with the card frontal to the illumination and the camera in Position 1. These data are used to evaluate the spatial uniformity of the illumination as discussed in Appendix A.

Record standard calibration data (pixel values). Replace Kodak 18% gray card with the Kodak standard card shown in Figure 8. Record an image with the sample holder oriented frontal to the lamp and the camera in Position 1.

¹³Kodak Gray Cards, Kodak Publication No. R-27.

Record sample calibration data. Replace standard card with sample and place grid (fiducial marker) on sample as shown in Figure 9. Record eight images corresponding to the sample oriented toward the light source and in the direction of the seven camera positions. Replace camera with photometer in Position 1 and record the radiance values for each of the three marked positions on the sample and for each of the eight orientations of the sample.

Record sample images for camera in Position 1. Replace photometer with camera, remove grid from sample. Take all measurements needed for the camera in Position 1 (this stage, which consists of alternate steps of reorienting the sample and recording the image, is done automatically).

Move camera and record sample images for camera in Position 2.

Repeat for all seven camera positions.

Repeat measurements for anisotropic samples. For anisotropic samples, rotate the sample about its normal (by either 45 or 90 degrees depending on the structure) and record another 205 samples over the seven camera positions.

Get radiance measurements for calibration. Occasionally do a lamp calibration which requires getting photometer readings for the 18% gray card and 32 strips on the standard card. The measured radiance from the 18% gray card is used to estimate the irradiance for each lamp as discussed in the normalization step of Section 2.5.

Note that the camera and photometer switch positions several times and at first glance it may seem that reordering the steps of the procedure would reduce this problem. However, the particular ordering of steps as listed is necessary. For instance, the aperture must be set with no grid on the sample (because the grid reduces overall brightness) and the grid cannot be removed between photometer and camera measurements (otherwise the fiducial markers would move).

2.5 Postprocessing

Here are the main steps in postprocessing.

Calibration. Transform pixel values to radiance as described in Section 2.3.

Segmentation. Segmentation simply requires identifying the part of the image in which the sample resides. Such segmentation is necessary so that the region for averaging can be identified for computing the BRDF. This is done by manually clicking on a subset of the corner points and using those values (along with the known sample orientation in each image and an orthographic projection assumption) to compute the transformations necessary to find the corner points of all the images in the sample measurement set. The resulting corner sets are manually inspected and adjusted when necessary to ensure that no background pixels are included in the measurements.

Normalization. An irradiance estimate is obtained using the radiance measured from the 18% Lambertian gray card. Specifically, the irradiance is the measured radiance multiplied by the factor $\pi/0.18$. Normalization by this estimated irradiance enables a BRDF estimate to be computed from the radiance values.

3. TEXTURE MEASUREMENTS

3.1 BTF Database

The appearance of a rough surface, whether manifested as a single radiance value or as image texture, depends on viewing and illumination directions. Just as the BRDF describes the coarse-scale appearance of a rough surface, the BTF (bidirectional texture function) is useful for describing the fine-scale appearance of a rough surface. Our measurements of image texture comprise the first BTF database for real-world surfaces. The database has over 14,000 images (61 samples, 205 measurements per sample, 205 additional measurements for anisotropic samples).

To illustrate the use of the BTF representation, Figure 11 shows rendered cylinders of plaster, pebbles, and concrete using two methods: ordinary 2-D texture-mapping and 3-D texture-mapping using the BTF measurement. Figure 12 shows similar renderings with crumpled paper, plush rug, and wood. The phrase “2-D texture-mapping” is used to refer to the warping or mapping of a single texture image onto an arbitrarily shaped object. For the 2-D texture-mapping examples in Figures 11 and 12, the texture image is taken as the frontally viewed image with the illumination direction at an angle of 22.5° to the right. For the 3-D texture-mapping examples in Figures 11 and 12, 13 images per sample are used from the database collection of 205 images. Of these 13 images, one view is the frontal view and the rest are oblique views of the sample. More specifically, these 13 images correspond to orientations of the sample’s global surface normal in the plane of the viewing and illumination direction at intervals of 11.25 degrees with the camera in Position 1 (see Figure 4). We make a piecewise planar approximation of the cylinder so that each planar section corresponds to the viewing and illumination direction of one of the 13 images. Then a section of each image is pasted in its appropriate position with averaging of three pixels at the section borders to reduce the appearance of seams.

Clearly 2-D texture-mapping, as we have defined it, cannot account for the variations in texture appearance due to local shading, foreshortening, shadowing, occlusions, and interreflections. These complex photometric and geometric effects significantly change the appearance of the surface texture. By using several images for 3-D texture-mapping of the cylinder, we can incorporate these effects and substantially improve the image realism. Consider the renderings shown in Figures 11 and 12. The surface roughness of the cylinders rendered with 3-D texture-mapping is readily apparent, whereas the cylinders rendered with 2-D texture-mapping appear rather smooth.

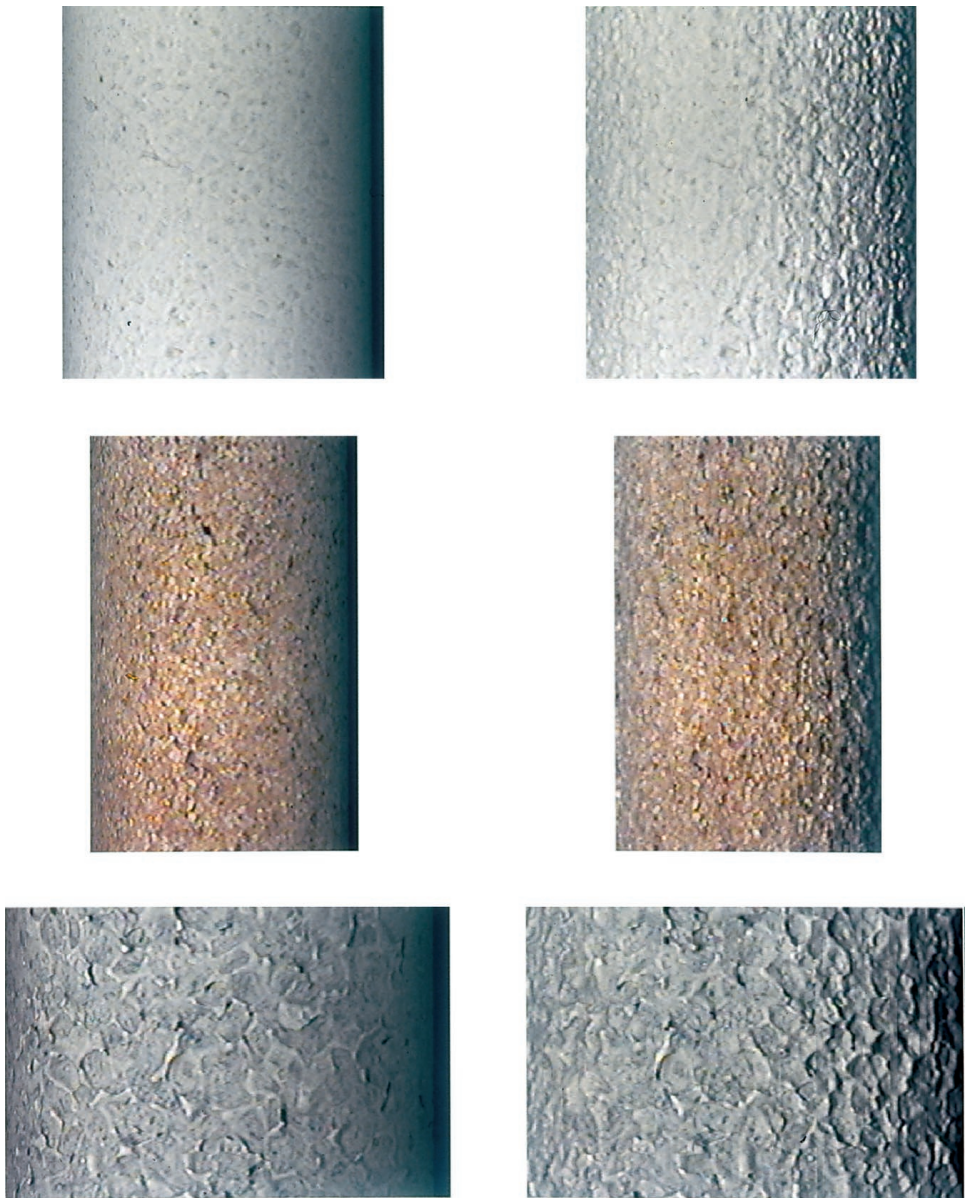


Fig. 11. Cylinders rendered with 2-D texture-mapping (left) and 3-D texture-mapping (right). From top to bottom, the samples rendered are Sample 11 (plaster), Sample 8 (pebbles), and Sample 45 (concrete).

These rendered cylinders demonstrate the potential of 3-D texture-mapping, but there are many unresolved issues. For instance, interpolation must be done between measured BTF images. Also, seams become a problem when the sizes of the characteristic texture elements become large

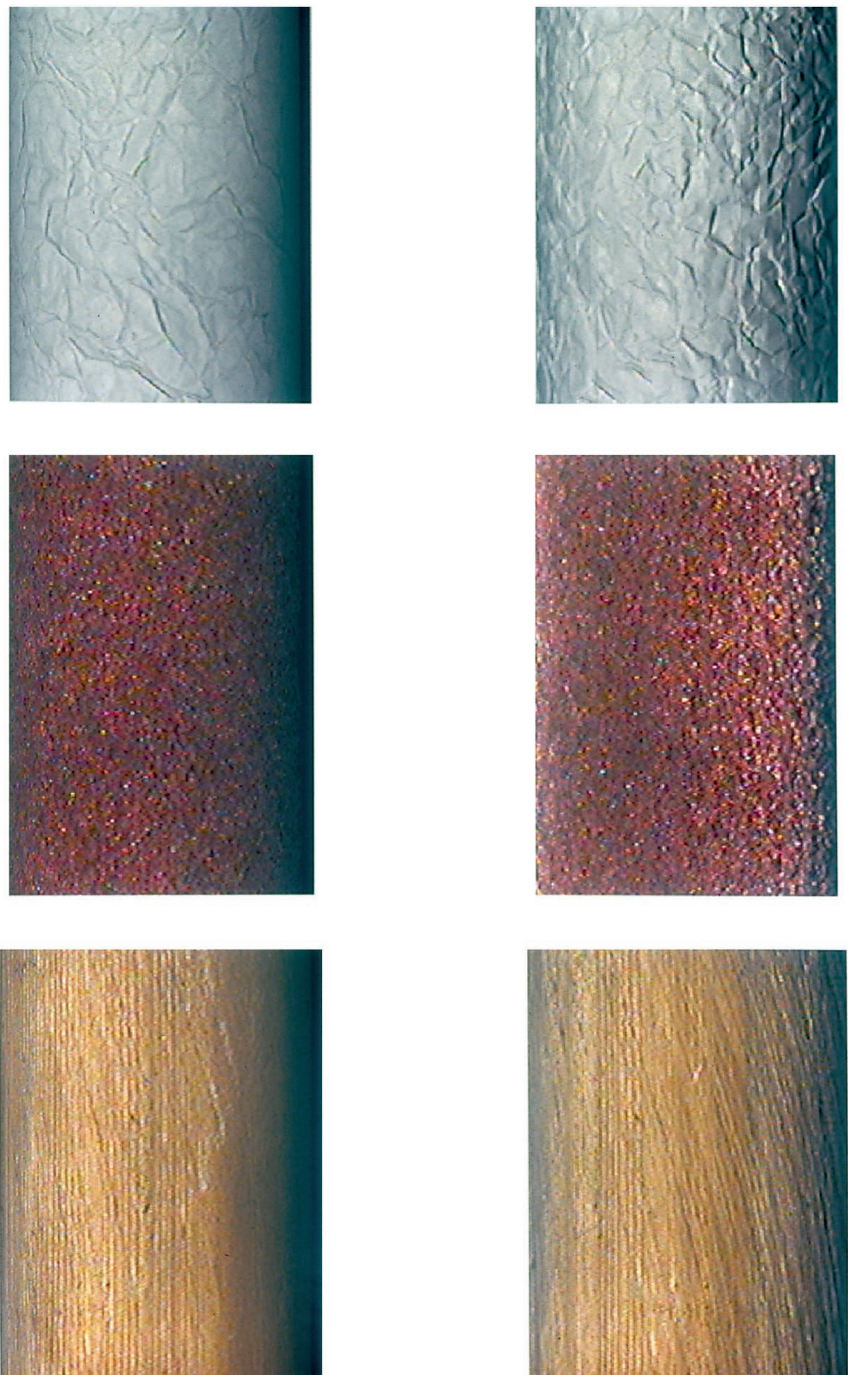


Fig. 12. Cylinders rendered with 2-D texture-mapping (left) and 3-D texture-mapping (right). From top to bottom, the samples rendered are Sample 28 (crumpled paper), Sample 19 (plush rug), and Sample 56 (wood).

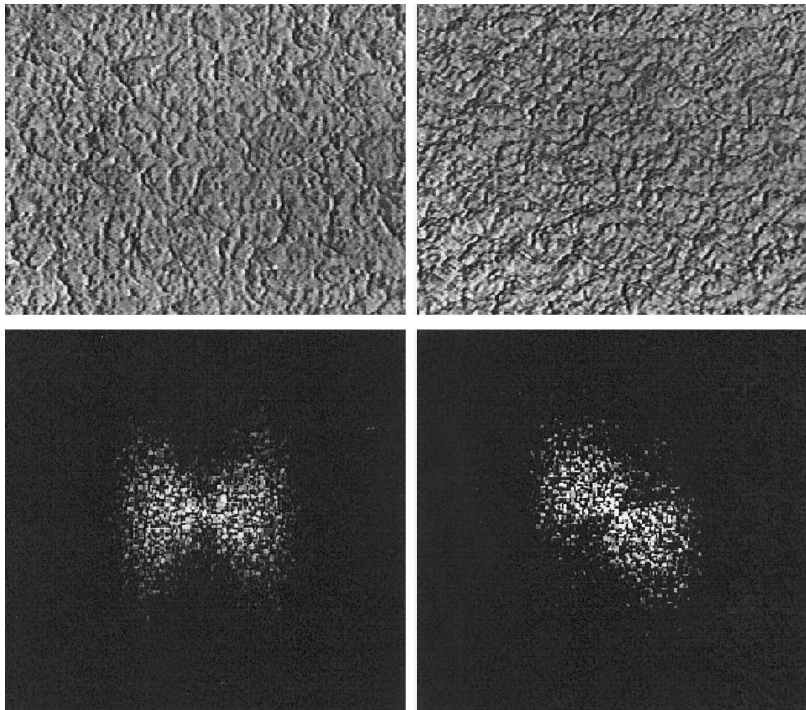


Fig. 13. Changes in the spatial spectrum due to changes in imaging conditions. (Top row) Two images of Sample 11 with different illumination and viewing directions. (Bottom row) Spatial spectrum of the images in the top row, with zero frequency at the center and brighter regions corresponding to higher magnitudes. The orientation change in the spectrum is due to the change of illumination direction which causes a change in the shadow direction.

compared to the size of the patch being textured. The database presented here is a starting point for further exploration into this area.

Important observations of the spatial-spectral content of image texture can be made using the BTF database. Consider the same sample shown under two different sets of illumination and viewing directions in Figure 13. The corresponding spatial Fourier spectra are also shown in Figure 13. Notice that the spectra are quite different. Most of the difference is due to the change in azimuthal angle of the illumination direction which causes a change in the shadowing direction and hence a change in the dominant orientation of the spectrum. If the image texture were due to a planar albedo or color variation, changes in the illumination direction would not have this type of effect on the spectrum. Source direction changes would only cause a uniform scaling of the intensity over the entire image. These observations have important implications in computer vision because texture recognition algorithms are often based on the spectral content of image textures. For recognition of real-world surfaces, invariant of illumination, and viewing direction, the BTF must be considered.

4. BRDF MEASUREMENTS

4.1 Comparison with Other BRDF Measurement Systems

BRDF measurement systems come in a wide variety of sizes and configurations. In the field of optical engineering, the apparatus is designed to measure effects of microscopic roughness from contaminants and thus the field of view can be quite small. For remote-sensing, the surface unit measured can be quite large as the systems are designed to measure large patches of terrestrial surfaces [Sandmeier et al. 1995]. Our system is designed to operate in a range that is useful for measuring the variety of surfaces that are of interest in computer graphics. As mentioned, the surface patch over which the BRDF is computed is approximately $10 \times 12\text{cm}$ and planar samples of this size for the variety of real-world surfaces shown in Figure 7 are relatively easy to obtain. Images of this size are sufficiently large to capture the characteristic surface variations of the texture of each of these surfaces.

The components of the BRDF measurement system vary also. The type of light sources varies from system to system and is often either a halogen source [Stavridi et al. 1997; Ward 1992] or a laser source [Marx and Vorburger 1989]. In some cases polarized light is used [Betty et al. 1996]. In some systems, mirrors are used to orient the incoming light [Marx and Vorburger 1989; Betty et al. 1996]. In other systems, especially when the sample must stay fixed (as in measurement of terrain for remote-sensing), a goniometer is used to orient the light source and detector [Sandmeier et al. 1995]. A goniometer consists of two arcs with a varying azimuth angle, one for the detector and one for the light source (if an artificial light source is used). In most cases the detector is some type of photometer, but in some apparatus, the detector is a CCD camera [Ward 1992; Karner et al. 1996]. One system allows the simultaneous capture of the hemisphere of scattering directions by using a hemispherical mirror and a fish-eye lens [Ward 1992].

Our measurement apparatus is driven by the goal of also measuring bidirectional texture. To achieve that goal, a CCD camera is our main sensor element. Some of the sources of error in our procedure (see Appendix B) are attributable to the imperfect calibration of CCD pixel to radiance values. Therefore other BRDF measurement systems may have better accuracy. However our system's simplicity and its suitability for simultaneous BRDF and BTF measurements make it ideal for our purposes.

Variations of BRDF measurement techniques as described and observation of sources of error among different BRDF measurements led to the development of the ASTM standard [ASTM]. For a discussion of our BRDF measurement apparatus and method in the context of the ASTM standard, see Appendix E.

4.2 BRDF Database

The BRDF measurements form a database with over 14,000 reflectance measurements (61 samples, 205 measurements per sample, 205 additional

measurements for anisotropic samples). This entire set is available electronically. The measured BRDFs are quite diverse and reveal the complex appearance of many ordinary surfaces.

Figures 14 and 15 illustrate examples of spheres rendered with the measured BRDF as seen from camera position 1, that is, with illumination from 22.5° to the right. Interpolation is used to obtain a continuous radiance pattern over each sphere. The rendered sphere corresponding to velvet (Sample 7) shows a particularly interesting BRDF that has bright regions when the global surface normal is close to 90 degrees from the illumination direction. This effect can be accounted for by considering the individual strands comprising the velvet structure that reflect light strongly as the illumination becomes oblique. This effect is consistent with the observed brightness in the interiors of folds of a velvet sheet. Indeed, the rendered velvet sphere gives a convincing impression of velvet.

The rendered spheres of plaster (Sample 30) and roofing shingle (Sample 32) show a fairly flat appearance which is quite different from the Lambertian prediction for such matte objects, but is consistent with Nayar and Oren [1995] and Oren and Nayar [1995]. Concrete (Sample 49) and salt crystals (Sample 43) also show a somewhat flat appearance, whereas rough paper (Sample 31) is more Lambertian. The plush rug (Sample 19) and moss (Sample 61) have similar reflectance patterns as one would expect from the similarities of their geometry. Rendered spheres from two anisotropic samples of wood (Sample 54 and Sample 56) are also illustrated in Figures 14 and 15. The structure of the anisotropy of sample 54 consists of horizontally oriented ridges. This ridge structure causes a vertical bright stripe instead of a specular lobe in the rendered sphere. Sample 56 shows a similar effect, but the anisotropic structure for this sample consists of near vertical ridges. Consequently, the corresponding rendered sphere shows a horizontal bright region due to the surface geometry.

5. ADDITIONAL INFORMATION

The BRDF measurements and BTF texture images are too numerous for inclusion in this article. The website (www.cs.columbia.edu/CAVE/curet) serves as a complement to this article and readers can access both databases electronically.

6. IMPLICATIONS FOR GRAPHICS

Our BRDF and BTF measurement databases together represent an extensive investigation of the appearance of real-world surfaces. Each of these databases has important implications for computer graphics.

Our BTF measurement database is the first comprehensive investigation of texture appearance as a function of viewing and illumination directions. As illustrated in Figures 11 and 13, changes of view and illumination cause notable effects on texture appearance that are not considered by current texture rendering algorithms. When the surface is rough, standard texture rendering tends to be too flat and unrealistic. Even if the rendering from a



Fig. 14. Spheres rendered using the BRDF measurements obtained from camera position 1 (illumination at 22.5° to the right). Interpolation was used to obtain radiance values between the measured points.

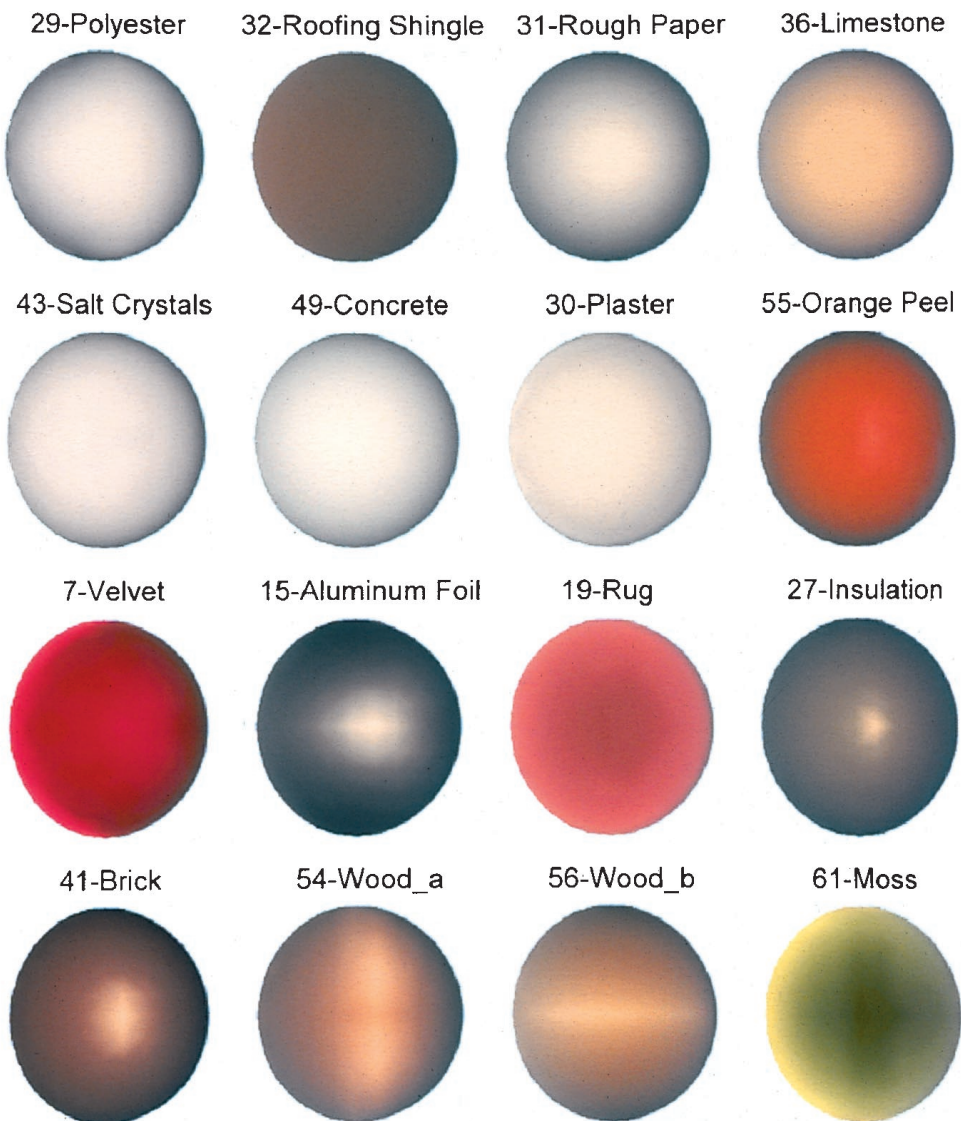


Fig. 15. Enlarged view of selected spheres (from Figure 14) rendered using the BRDF measurements obtained from camera position 1 (illumination at 22.5° to the right). Interpolation was used to obtain radiance values between the measured points.

single view is suitably realistic, the realism is lost when the view or illumination changes. The database illustrates the need for 3-D texture rendering algorithms and serves as a starting point for their exploration.

Our BRDF measurement database provides a thorough investigation of the reflectance properties of real-world rough surfaces. This database fills a long-standing need for a benchmark to test and compare BRDF models as

we have done in Dana et al. [1997] for the Oren–Nayar [1995] model and the Koenderink et al. [1996] decomposition. Such a comparison is useful in choosing a representation that has the right balance of accuracy and compactness for the application at hand. In circumstances that necessitate the use of a less accurate reflectance model, such as the Lambertian model, the database provides a means of gauging expected errors.

APPENDIX A. Light Sources

Because of the limited lifetime of the lamps employed in the measurements, three different lamps were used:

- Lamp 1 was used for Samples 1–8.
- Lamp 2 was used for Samples 9–44.
- Lamp 3 was used for Samples 45–61.

Each of these lamps was operated with a regulated power supply.

Periodically during the measurements we performed a *lamp calibration* which consisted of placing the photometer region of interest over each strip on the Kodak standard card. This card consisted of 20 gray strips (strip no. 0–19), a piece of a standard 18% gray card (strip no. 20) that was attached at the center of the card, and 12 color strips (strip no. 21–32). The main purpose of these lamp calibrations was to relate pixel values to radiance values as described in Section 2.3. (An image of the Kodak standard card was obtained for each sample after the camera aperture was set). The second purpose of the lamp calibrations was to determine the temporal stability of the lamp (whether it remained at approximately the same brightness for each day of the experiment).

For lamp 1, two calibrations were performed on Day 1 and Day 4 of the measurements. Sample 1 was measured on Day 1 and sample 8 was measured on Day 4. Figure 16 shows the 33 photometer measurements from the standard calibration card for each of the lamp calibrations.

For lamp 2, four calibrations were done on Days 5, 6, 11, and 13. Sample 9 was measured on Day 3 and sample 44 measured on Day 14. Figure 17 shows the 33 photometer measurements from the standard calibration card for each of the lamp calibrations.

For lamp 3, calibrations were done on Days 18 and 22. Sample 45 was measured on Day 15 and Sample 61 was measured on Day 22. Figure 18 shows the 33 photometer measurements from the standard calibration card for each of the lamp calibrations.

The plots from the three lamps show that temporal stability is reasonable especially for the gray strips. The temporal change in lamp 2 is larger in the colored reference strips. This observation suggests that the illumination spectrum also changes with time. Since most of the samples are broadband rather than monochrome, the small decrease in the gray calibration strips suggests that the temporal stability is adequate.

Using the photometer measurements from the 18% Lambertian gray card the irradiance was estimated. For lamps 1, 2, and 3 the irradiance in

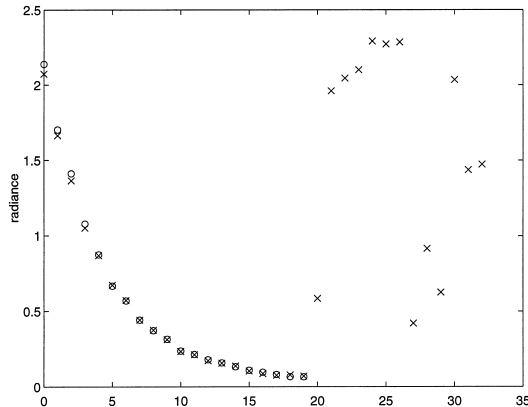


Fig. 16. Lamp 1 calibration data. The first 20 points are the measured radiance from gray strips on the Kodak standard card. The last 13 points are the measured radiance from the 18% gray card followed by the 12 color strips on the Kodak 18% Gray Card. The lamp calibration was repeated twice on separate days. Data from the first set are plotted with the symbol "o". Data from the second set are plotted with the symbol "x". (In this case the first calibration did not include the colored strips.)

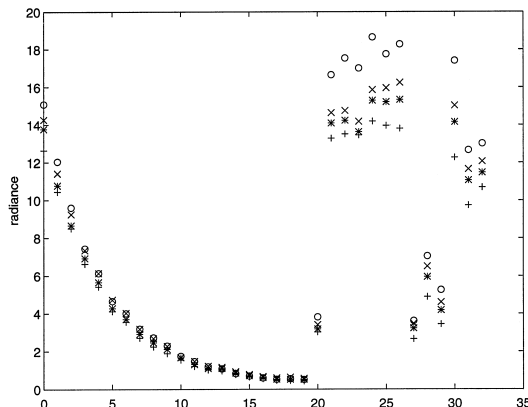


Fig. 17. Lamp 2 calibration data. The first 20 points are the measured radiance from gray strips on the Kodak standard card. The last 13 points are the measured radiance from the 18% gray card followed by the 12 color strips on the Kodak standard card. The lamp calibration was repeated four times on separate days. Data from the first, second, third, and fourth calibrations are plotted with the symbols "o", "x", "*", and "+", respectively. Notice a small decrease in the lamp brightness with time.

watts/meter² integrated over the wavelength range of 380nm to 780nm is shown in Table I.

The spatial uniformity of the lamps was analyzed by obtaining images of a Kodak 18% gray card with frontal illumination viewed at an angle of 22.5 degrees (i.e., with the camera in position 1) with the aperture set for the current sample. To summarize the result, we used one gray card image for each lamp (specifically we used the gray card images obtained when samples 8, 25, and 47 were measured). The gray card images were normal-

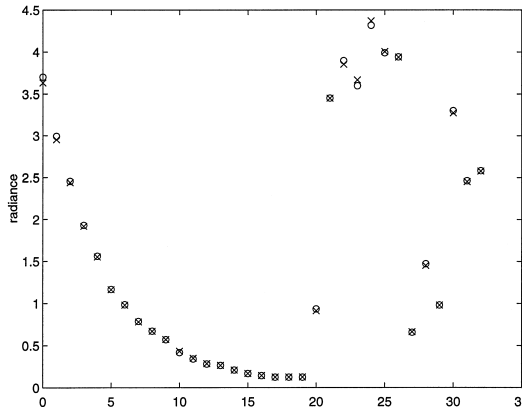


Fig. 18. Lamp 3 calibration data. The first 20 points are the measured radiance from gray strips on the Kodak standard card. The last 13 points are the measured radiance from the 18% gray card followed by the 12 color strips on the Kodak standard card. The lamp calibration was repeated twice on separate days. Data from the first set are plotted with the symbol “o”. Data from the second set are plotted with the symbol “x”.

Table I. Estimated Irradiance and Standard Deviation of the Normalized Gray Card Image

| Lamp | Irradiance | σ_r | σ_g | σ_b |
|------|------------|------------|------------|------------|
| 1 | 9.56 | 0.0631 | 0.0620 | 0.0666 |
| 2 | 57.664 | 0.0594 | 0.0605 | 0.0615 |
| 3 | 13.0799 | 0.0496 | 0.0496 | 0.0529 |

ized so that the maximum value was 1 and the standard deviation across the normalized card for each RGB channel (σ_r , σ_g , σ_b) was computed. The results are shown in Table I.

APPENDIX B. Sources of Error

Nonlinearities in relationship between pixels and radiance. The calibration scheme described in Section 2.3 relies on an underlying linear relationship between radiance and pixel values. This linear approximation is good for most samples and for most of the operating range, as indicated in the calibration curves of Appendix C. However, the approximation becomes poor for low and high radiance values. In addition, pixel underflow and overflow, that is, pixels which are clipped to values of 0 or 255 by digitization, contribute significantly to this nonlinearity. For each sample, the camera aperture and in some cases the camera gain were adjusted to reduce the amount of pixel overflow or underflow. But these adjustments did not remove this source of error completely.

Camera positioning error. The camera tripod was manually positioned into holders attached to the lab floor that marked the seven camera positions shown in Figure 4. This camera positioning was not exact and caused a shift in the image centers.

Gaussian estimate of camera response. For color calibration, as described in Section 2.3, the camera response was approximated by Gaussian response curves. The actual camera response was unknown and therefore this approximation may be a source of error.

Variable thickness of sample. This variable thickness was partially accounted for by changing robot calibration parameters.

Visibility of sample base in some semi-transparent samples. Specifically, frosted glass, polyester, cotton, and the peacock feather were semitransparent and the backing (either cardboard or the wooden sample base painted in matte black) was slightly visible through these samples. For the peacock feather, the glue used to attach the sample was visible.

Global shape of some samples. Orange peel, tree bark, and straw were not globally planar in shape. (Tree bark was not flat at all. Orange peel was as flat as we could make it. The bundle of straw was attached by tape at either end giving it some curvature.)

Robot errors. Based on the manufacturer's specifications and our observations, we estimate that the systematic angular errors are about one degree and the nonsystematic errors are on the order of a tenth of a degree.

Stray light in room. The room had light colored walls. The windows and doors were blocked to control ambient light. The lamp was positioned so that there was no wall in the illumination path for about 6 meters. We expected the stray light to be quite small.

Spatial uniformity of lamp. See Section A for a discussion of the spatial uniformity of each lamp.

Lamp beam not perfectly parallel. Although the exact deviation from parallel light was not measured precisely, we estimated the deviation to be on the order of a few degrees.

Time-varying illumination. See Appendix A for a discussion of the temporal stability of the lamps. The decrease in lamp brightness with time had some effect on the calibration results. The decrease was small in the gray-colored reference strips and somewhat larger in the colored reference strips. This observation suggests that the illumination spectrum also changes with time. Since most of the samples are broadband rather than monochrome the small decrease in the gray calibration strips suggests that the temporal stability is adequate.

Angle error due to extended flat sample. Because the sample has an extended area, there was a slight error (about 1.5 degrees) in the viewing angle away from the center of the sample.

Spurious specular reflectance. A source of error in the experiments occurred because of a brightness decrease present in the images when the robot edges specularly reflect the incident light. Although the camera's gain and gamma correction were turned off, a decrease in brightness of about

10% was noticed in these specular and near-specular positions. On average, this decrease affected 15 of the 205 images obtained for each sample. By analyzing these images, it became clear that the empty image background around the sample provided a cue for when the brightness decrease occurred and the magnitude of that decrease. (By “empty background” we mean there was no significant reflection since the only object was a relatively distant wall.) The relation between the background pixel value and the intensity dip was approximately independent of the aperture and light source since it depended only on the dark current of the camera. By comparing the average background pixel value for images with no apparent brightness decrease with the average background pixel value for images with a brightness decrease, a threshold value of 7 was determined. Images with average background pixels below threshold had a brightness decrease.

A correction procedure was devised by using the samples that were measured twice at two different magnifications (samples 2, 11, 12, and 14). The zoomed view of these samples did not show the robot edges and therefore the brightness decrease did not occur. These samples provided ground truth to determine the exact magnitude of the brightness attenuation and to determine the relationship between the brightness attenuation and the average background pixel value. The correction procedure is as follows.

- (1) Manually segment the background in the specular and near-specular images to obtain an average background value B .
- (2) If the average background pixel value is less than the threshold of 7, divide the image by a correction factor $c = 0.0360B + 0.7236$.

The technical report [Dana et al. 1996] has a list of the images that were corrected with the corresponding correction factor (applied to RGB).

APPENDIX C. Calibration Plots

The calibration plots for some of the samples are shown in this appendix. The remainder of the calibration plots are given in Dana et al. [1996]. These plots show the estimated linear relationship between radiance and pixel values. The plots also show the sample calibration data and standard calibration data used to estimate this linear relationship. These plots are useful for evaluating the quality of the gray and color calibrations for each sample. See Figures 19 and 20.

APPENDIX D. Verification

To provide some verification that the measured results are physically plausible we conducted a test of the Helmholtz reciprocity principle. According to this principle the BRDF should remain the same if the illumination and viewing angles are switched. For our measurement configuration, there were several positions where the illumination and viewing directions were effectively switched. To test reciprocity, we chose 25 of the samples which seemed most isotropic based on visual inspection. These sample numbers are 2, 4, 6, 8, 9, 11, 12, 14, 15, 16, 17, 20, 21, 25, 28, 29, 30,

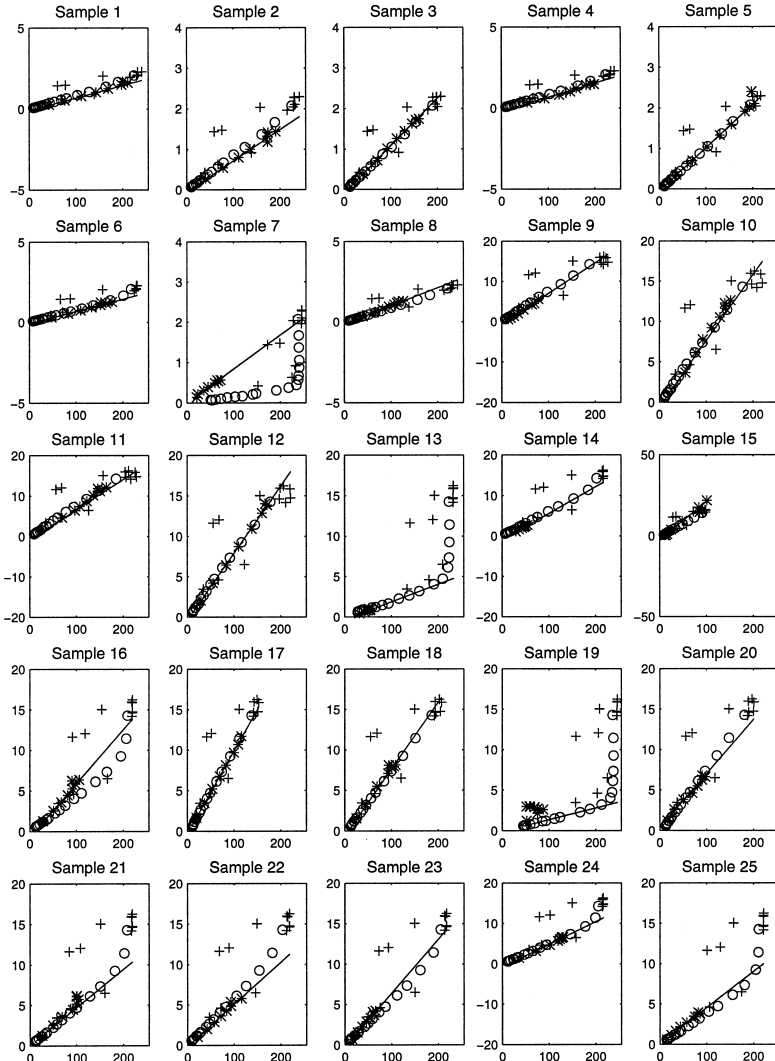


Fig. 19. Calibration plots for the gray calibration data for Samples 1–25. The plots show pixel value (abscissa) and radiance measured by the photometer (ordinate). The sample calibration data are plotted with the symbol “*”. The gray strips from the standard calibration data are plotted with the symbol “o”, and the colored strips from the standard calibration data are plotted with the symbol “+”. The estimated linear calibration function is plotted with a solid line.

31, 32, 35, 37, 41, 43, 47, and 49. Of the 205 different illumination and viewing directions, eight pairs were chosen which differed by a swapping of the illumination and viewing polar angles. An additional criterion for choosing these eight pairs was to include only those pairs with polar angles less than 75 degrees (larger polar angles showed more deviation from the reciprocity principle but also suffered from additional errors such as pixel

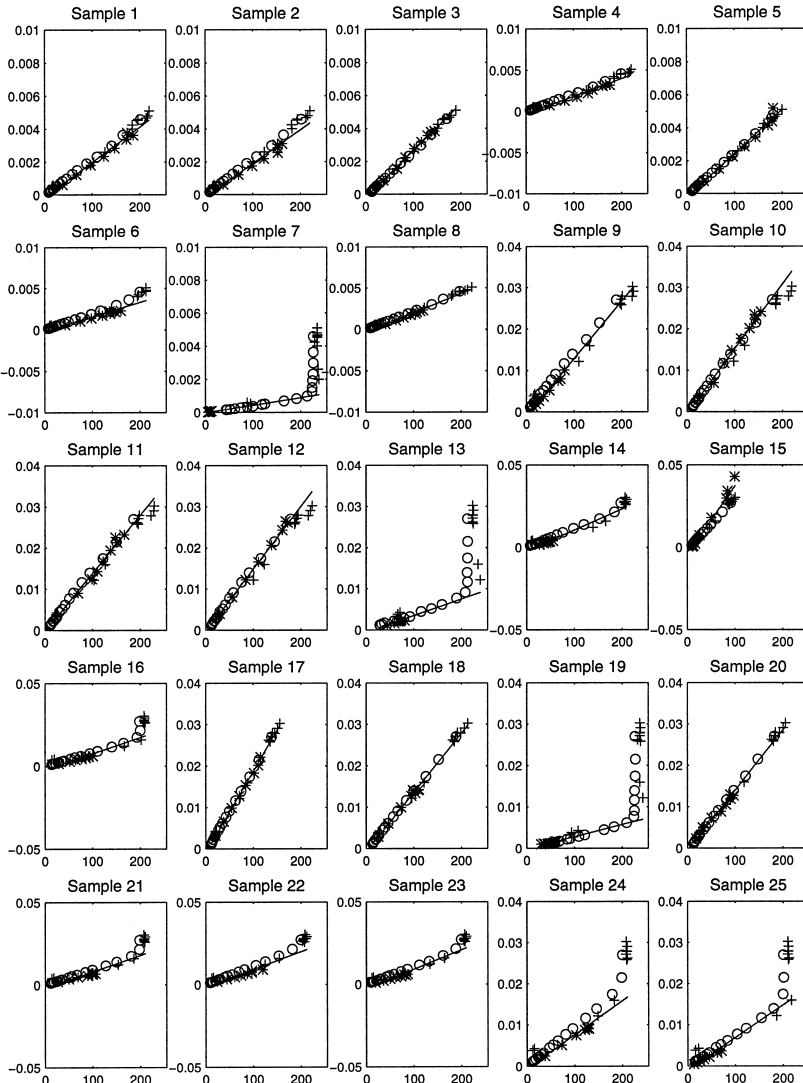


Fig. 20. Calibration plots for the green calibration data for Samples 1–25. The plotting symbols are described in Figure 19.

overflow or underflow). Using the numbers 1 to 205 to denote each measurement position, the eight chosen pairs were: (33 47), (42 52), (49 55), (73 100), (90 102), (119 141), (136 125), and (156 165). The average normalized mean square error was 3% for the BRDFs obtained with gray calibration, and 3.6%, 5.0%, and 5.6% for the red, green, and blue components, respectively, for the BRDFs obtained with color calibration. These small error values indicate that the measurements approximately satisfy the reciprocity condition.

APPENDIX E. ASTM Standard

Variations of BRDF measurement techniques as described and observation of sources of error among different BRDF measurements led to the development of the ASTM standard [ASTM]. In this section, we discuss our BRDF measurement equipment and method in the context of the ASTM standard. The purpose of this discussion is to enable evaluation of the sources of error in our BRDF measurements and determine whether the accuracy is sufficient for the reader's purposes.

Appendix E.1 Apparatus

The ASTM standard [ASTM] outlines a standard practice for BRDF measurement. To compare our measurement equipment with the standards proposed by ASTM, we iterate through each item in the apparatus section (Section 5 of ASTM) and discuss the relevant item of our measurement system in the context of the standard's recommendations.

Source assembly. Our source assembly consisted of a halogen lamp in the focal point of a large Fresnel lens to obtain approximately uniform irradiation with a beam of 30cm diameter. Although the exact deviation from parallel light was not measured precisely, we estimated the deviation to be on the order of a few degrees. Three different lamps were used in the course of the measurements because of the finite lifetime of each lamp. Spatial uniformity was evaluated for each lamp as described in Appendix A. The standard says that if a broadband source is used, the wavelength selection technique should be specified. Indeed our source was broadband; however wavelength selection is inherent in the camera response of the RGB CCD camera. As is typical, baffling and a spatial filter were used around the fixed source assembly to limit off-axis light as depicted in Figure 2. The standard recommends that a means be provided for controlling the polarization state of the incident flux. In our procedure, we did not polarize the light in any manner.

Sample Holder. Our sample holder was attached to the robot manipulator and is depicted in Figure 2. The robotics provided means for orienting the sample as described in the standard. The standard also mentions that the sample holder may have an x - y stage for scanning the surface. Since a CCD camera was used as the detector, and the entire sample was visible in the field of view of the camera, no such scanning was necessary. The standard states that the sample mount should not contribute any stray flux; our sample mount did have metallic edges that may have contributed some stray flux and was a source of error in the experiment (see Appendix B).

Receiver Assembly. The receiver assembly consists of a 3-CCD camera (separate CCD for each of the RGB components) mounted on a tripod. The tripod was positioned by wooden holders attached to the floor of the lab. Seven positions were made on the floor of the lab (as illustrated in Figure 4). The wooden holders did change in integrity over the course of the experiment, and the process of lifting and moving the tripod did have the

effect of changing its configuration slightly. Therefore there were some variations in the actual position of the camera. These variations were reduced to some extent by placing the tripod while visually centering the correctly oriented sample in the field of view. The camera orientation during measurements was always parallel to the floor. Out-of-plane of incidence measurements were obtained by orienting the sample as described in Section 2.1.

Although the CCD is the main sensor or receiver, the photometer is the receiver during part of the calibration stage. During this stage, the photometer mounted on a tripod was placed in the wooden holders for camera position 1 (22.5 degrees adjacent to the light source as depicted in Figure 4).

According to the standard, the acceptance aperture of the receiver should be well defined if the solid angle subtended by the receiver aperture stop from the sample is used in BRDF calculation. In our case, the BRDF was computed as the measured radiance divided by irradiance. The measured radiance was obtained by converting average pixel values to radiance as described in Section 2.3. Since the photometer output was in units of radians/(meter² – steridian), the acceptance angle was implicitly included. The irradiance estimate was obtained by measuring the radiance from a Lambertian reference sample frontally illuminated. Specifically the Kodak 18% gray card described in Section 2.4 served as the reference sample with a BRDF given by $0.18/\pi$. By multiplying the radiance measured from the gray card by $\pi/0.18$, an irradiance estimate was obtained. Since three lamps were used in the experiment, three different irradiance values were computed as indicated in Table I.

The acceptance aperture of the camera was variable but this variation was captured in the calibration parameters that differed for each sample.

The standard mentions speckle as a potential problem, but since we did not use a coherent source this was not an issue.

Beam dump. Beam dumps can be used to trap specular reflection from the sample so that it does not contribute to measured reflectance via wall reflections. These were not employed in our setup.

Source monitor. A regulated voltage source was employed in our setup for a stable light source. Long-term fluctuations in the source intensity were measured by calibrations done over the course of the experiment (see Appendix A). No additional source monitor was included in our equipment.

Appendix E.2 Calibration and Normalization

To compare our calibration and normalization with the standards proposed by ASTM, we discuss our methods in the context of the standard's recommendations outlined in the calibration and normalization section (Section 6 of ASTM).

Instrument calibration. The standard says that system nonlinearity is a major contributor to error. Indeed our system has nonlinearity for these major reasons.

- (1) The linear relationship between radiance and intensity is only an approximation.
- (2) Pixel underflow exists because of the finite 8-bit precision of the digital measurements.
- (3) Pixel overflow exists because of the finite 8-bit precision of the digital measurements.

Calibration curves. Calibration curves such as the one described in the standard are needed to describe optical power versus voltage. The attenuation method we chose to obtain our calibration curve was the sequence of grayscale strips of the Kodak standard card as described in Section 2.3. Our calibration curves were plots of radiance versus attenuation obtained by measuring these gray strips. The standard card has 20 gray strips with 0.1 density increments and relative density values from a nominal “white” of approximately 0.05 (90% reflectance) to 1.95 (1% reflectance). The photometer was used to record radiance from each of these strips and the CCD camera used to image these strips for every sample (since camera gain or aperture may change from sample to sample).

Electronic noise. The electronic noise in our system was considered small enough to neglect.

Calibration checks. Calibration checks were accomplished by repeating the lamp calibration several times over the measurements as described in Appendix A.

Normalization. The standard presents four methods of normalizing to compute the BRDF. We employed the *relative BRDF* method for normalization. In this method a reference sample with known BRDF is used and, as mentioned, the 18% Kodak Gray Card serves this purpose.

REFERENCES

- ASTM. Standard E1392-90, Standard practice for angle resolved optical scatter measurements on specular or diffuse surfaces. American Society for Testing and Materials.
- BECKER, B. G. AND MAX, N. L. 1993. Smooth transitions between bump rendering algorithms. *Comput. Graph. SIGGRAPH 93*, 27, (Aug.), 183–190.
- BETTY, C. L., FUNG, A. K., AND IRONS, J. 1996. The measured polarized bidirectional reflectance distribution function of a spectralon calibration target. In *Proceedings of IGARSS '96, IEEE International Geoscience and Remote Sensing Symposium* (Lincoln, NE, May 27–31) 2183–2185.
- BLINN, J. F. 1977. Models of light reflection for computer synthesized pictures. *Comput. Graph. SIGGRAPH 77*, 11, (July), 192–198.
- BLINN, J. F. 1978. Simulation of wrinkled surfaces. In *Proceedings of SIGGRAPH 78*, 286–292.
- BORN, M. AND WOLF, E. 1959. *Principles of Optics*, Pergamon, New York.
- CHATTERJEE, S. 1993. Classification of natural textures using Gaussian Markov random fields. In *Markov Random Fields: Theory and Applications*, Academic Press, Boston, 159–177.
- DANA, K. J. AND NAYAR, S. K. 1998. Histogram model for 3D textures. In *Proceedings of the IEEE Conference on Computer Vision and Pattern Recognition* (Santa Barbara, CA, June 23–25), 618–624.

- DANA, K. J., VAN GINNEKEN, B., NAYAR, S. K., AND KOENDERINK, J. J. 1996. Reflectance and texture of real-world surfaces. Columbia University, Tech. Rep. CUCS-048-96, Dec.
- DANA, K. J., VAN GINNEKEN, B., NAYAR, S. K., AND KOENDERINK, J. J. 1997. Reflectance and texture of real world surfaces. In *Proceedings of the IEEE Conference on Computer Vision and Pattern Recognition* (San Juan, PR, June 17–19), 151–157.
- DEBEVEC, P. E., TAYLOR, C. J., AND MALIK, J. 1996. Modeling and rendering architecture from photographs: A hybrid geometry and image-based approach. *Comput. Graph. SIGGRAPH 96* (Aug.), 11–20.
- VAN GINNEKEN, B., KOENDERINK, J. J., AND DANA, K. J. 1997. Texture histograms as a function of irradiation and viewing direction. *Int. J. Comput. Vis.* (to appear).
- VAN GINNEKEN, B., STAVRIDIS, M., AND KOENDERINK, J. J. 1998. Diffuse and specular reflectance from rough surfaces. *Appl. Opt.* 37 (Jan.), 130–139.
- GOURAUD, H. 1971. Continuous shading of curves surfaces. *IEEE Trans. Comput.* (June), 623–629.
- HECKBERT, P. S. 1986. A survey of texture mapping. *IEEE Comput. Graph. Appl.* 6 (Nov.), 56–67.
- HERREN, K. A. 1989. Measurements of polarization scattering in the vacuum ultraviolet. In *Polarization Considerations for Optical Systems II, Proceedings of the SPIE* (San Diego, CA, Aug. 9–11), Vol. 1166, 33–41.
- HOWARD, T. L., GEORGE, P. M., FLAMMANG, S., AND MOSSMAN, D. 1989. Vacuum BRDF measurements of cryogenic optical surfaces. In *Scatter from Optical Components, Proceedings of the SPIE* (San Diego, CA, Aug. 8–10), Vol. 1165, 350–359.
- HORN, B. K. P. AND BROOKS, M. J. 1989. *Shape from Shading*. MIT Press, Cambridge, MA.
- KARNER, K. F., MAYER, H., AND GERVAUTZ, M. 1996. An image based measurement system for anisotropic reflection. *Comput. Graph. Forum (EUROGRAPHICS '96)* 15, 3 (Aug.), 119–28.
- KASHYAP, R. L. 1984. Characterization and estimation of two-dimensional ARMA models. *IEEE Trans. Inf. Theor. IT-30*, 5 (Sept.), 736–745.
- KOENDERINK, J. J. AND VAN DOORN, A. J. 1996. Illuminance texture due to surface meso-structure. *J. Opt. Soc. Am. A* 13, 3, 452–463.
- KOENDERINK, J. J., VAN DOORN, A. J., AND STAVRIDIS, M. 1996. Bidirectional reflection distribution function expressed in terms of surface scattering modes. In *Proceedings of the European Conference on Computer Vision*, vol. 2, 28–39.
- KOENDERINK, J. J., VAN DOORN, A. J., DANA, K. J., AND NAYAR, S. K. 1998. Bidirectional reflection distribution function of thoroughly pitted surfaces. *Int. J. Comput. Vis.* (to appear).
- KRUMM, J. AND SHAFER, S. A. 1995. Texture segmentation and shape in the same image. In *Proceedings of the IEEE Conference on Computer Vision* (Cambridge, MA, June 20–23), 121–127.
- LEUNG, T. AND MALIK, J. 1997. On perpendicular texture: Why do we see more flowers in the distance? In *Proceedings of the IEEE Conference on CVPR* (San Juan, PR, June 17–19), 807–813.
- LEWIS, J. P. 1989. Algorithms for solid noise synthesis. *Comput. Graph.* 23, 3 (July), 263–270.
- LI, Z., FUNG, A. K., GIBBS, D., BETTY, C. L., TJIUATJA, S., AND IRONS, J. R. 1994. A modeling study of bidirectional reflectance from soil surfaces. In *Proceedings of IGARSS '94, IEEE International Geoscience and Remote Sensing Symposium* (Pasadena, CA, Aug. 8–12), 1835–1837.
- MARX, E. AND VORBURGER, T. V. 1989. Light scattered by random rough surfaces and roughness determination. In *Scatter from Optical Components, Proceedings of the SPIE* (Aug.), Vol. 1,165, 72–86.
- NAYAR, S. K. AND OREN, M. 1995. Visual appearance of matte surfaces. *Science* 267 (Feb.), 1153–1156.
- NAYAR, S. K., IKEUCHI, K., AND KANADE, T. 1991. Surface reflection: Physical and geometrical perspectives. *IEEE Trans. Patt. Anal. Mach. Intell.* 13, 7 (July), 611–634.
- NICODEMUS, F. E. 1970. Reflectance nomenclature and directional reflectance and emissivity. *Appl. Opt.* 9, 1474–1475.

- NICODEMUS, F. E., RICHMON, J. C., HSIA, J. J., GINSBERG, I. W., AND LIMPERIS, T. 1977. Geometric considerations and nomenclature for reflectance. NBS Monograph 160, National Bureau of Standards, Washington, DC, Oct.
- NOLIN, A. W., STEFFEN, K., AND DOZIER, J. 1994. Measurement and modeling of the bidirectional reflectance of snow. In *Proceedings of IGARSS '94, IEEE International Geoscience and Remote Sensing Symposium* (Pasadena, CA, Aug. 8–12), 1919–1921.
- OREN, M. AND NAYAR, S. K. 1995. Generalization of the Lambertian model and implications for machine vision. *Int. J. Comput. Vis.* 14, 227–251.
- PATEL, M. A. S. AND COHEN, F. S. 1992. Shape from texture using Markov random field models and stereo-windows. In *Proceedings of the IEEE Conference on CVPR* (Champaign, IL, June 15–18), 290–305.
- PEACHEY, D. R. 1985. Solid texturing of complex surfaces. In *Proceedings of SIGGRAPH 1985, Comput. Graph.* 19, 279–286.
- PERLIN, K. 1985. An image synthesizer. *Comput. Graph.* 19, 3 (July), 287–296.
- PERLIN, K. 1989. Hypertexture. *Comput. Graph.* 23, 3 (July), 253–262.
- PICARD, R. W., KABIR, T., AND LIU, F. 1993. Real-time recognition with the entire Brodatz texture database. In *Proceedings of the IEEE Conference on CVPR* (New York, NY, June 15–17), 638–639.
- POULIN, P. AND FOURNIER, A. 1990. A model for anisotropic reflection. *Comput. Graph.* 24, 4 (Aug.), 273–282.
- SAKAS, G. AND KERNKE, B. 1994. Texture shaping: A method for modeling arbitrarily shaped volume objects in texture space. In *Photorealistic Rendering in Computer Graphics, Proceedings of the Second Eurographics Workshop on Rendering*, Springer-Verlag, New York, 206–218.
- SANDMEIER, S., SANDMEIER, W., ITTEN, K. I., SCHAEPMAN, M. E., AND KELLENBERGER, T. W. 1995. The Swiss field-goniometer system. In *Proceedings of IGARSS '95, IEEE International Geoscience and Remote Sensing Symposium* (July), 2078–2080.
- SCHLUESSEL, D., DICKINSON, R. E., PRIVETTE, J. L., EMERY, W. J., AND KOKALY, R. 1994. Modeling the bidirectional reflectance distribution function of mixed finite plant canopies and soil. *J. Geophys. Res.* 99, D5 (May), 10577–600.
- STAVRIDIS, M., VAN GINNEKEN, B., AND KOENDERINK, J. J. 1997. Surface bidirectional reflection distribution function and the texture of bricks and tiles. *Appl. Opt.* 36, 16 (June), 3717–3725.
- STOVER, J. C. 1989. Scatter from optical components: An overview. In *Scatter from Optical Components, Proceedings of the SPIE* (San Francisco, CA, Aug. 8–10), Vol. 1165, 2–9.
- SUEN, P. AND HEALEY, G. 1998. Analyzing the bidirectional texture function. In *Proceedings of the IEEE Conference on CVPR* (San Diego, CA, June 23–25), 753–758.
- SUPER, B. J. AND BOVIK, A. C. 1995. Shape from texture using local spectral moments. *IEEE Trans. Patt. Anal. Mach. Intell.* 17, 333–343.
- TAGARE, H. D. AND DEFIGUEIREDO, R. J. P. 1993. A framework for the construction of reflectance maps for machine vision. *CVGIP: Image Understand.* 57, 3 (May), 265–282.
- TORRANCE, K. E. AND SPARROW, E. M. 1967. Theory for off-specular reflection from roughened surfaces. *J. Opt. Soc. Am.* 57, 9, 1105–1114.
- WANG, L. AND HEALEY, G. 1996. Illumination and geometry invariant recognition of texture in color images. In *Proceedings of the IEEE Conference on CVPR* (San Francisco, CA, June 18–20), 419–424.
- WARD, G. J. 1992. Measuring and modeling anisotropic reflection. *Comput. Graph.* 26, 2, ACM SIGGRAPH (July), 265–272.
- WESTIN, S. H., ARVO, J. R., AND TORRANCE, K. E. 1992. Predicting reflectance functions from complex surfaces. *Comput. Graph.* 26, 2, ACM SIGGRAPH (July), 255–263.
- WOLFF, L. B. 1994. A diffuse reflectance model for smooth dielectrics. *J. Opt. Soc. Am. A—Special Issue on Physics Based Machine Vision* (Nov.), 2956–2968.
- WOODHAM, R. J. 1980. Photometric methods for determining surface orientation from multiple images. *Opt. Eng.* 19, 1, 139–144.
- XIE, Z. AND BRADY, M. 1996. Texture segmentation using local energy in wavelet scale space. *ECCV 1*, 304–313.

Received August 1997; revised March 1998; accepted October 1998

ACM Transactions on Graphics, Vol. 18, No. 1, January 1999.